Journal of Materials Chemistry C

Materials for optical, magnetic and electronic devices

rsc.li/materials-c

ROYAL SOCIETY
OF CHEMISTRY

10 YEARS ANNIVERSARY
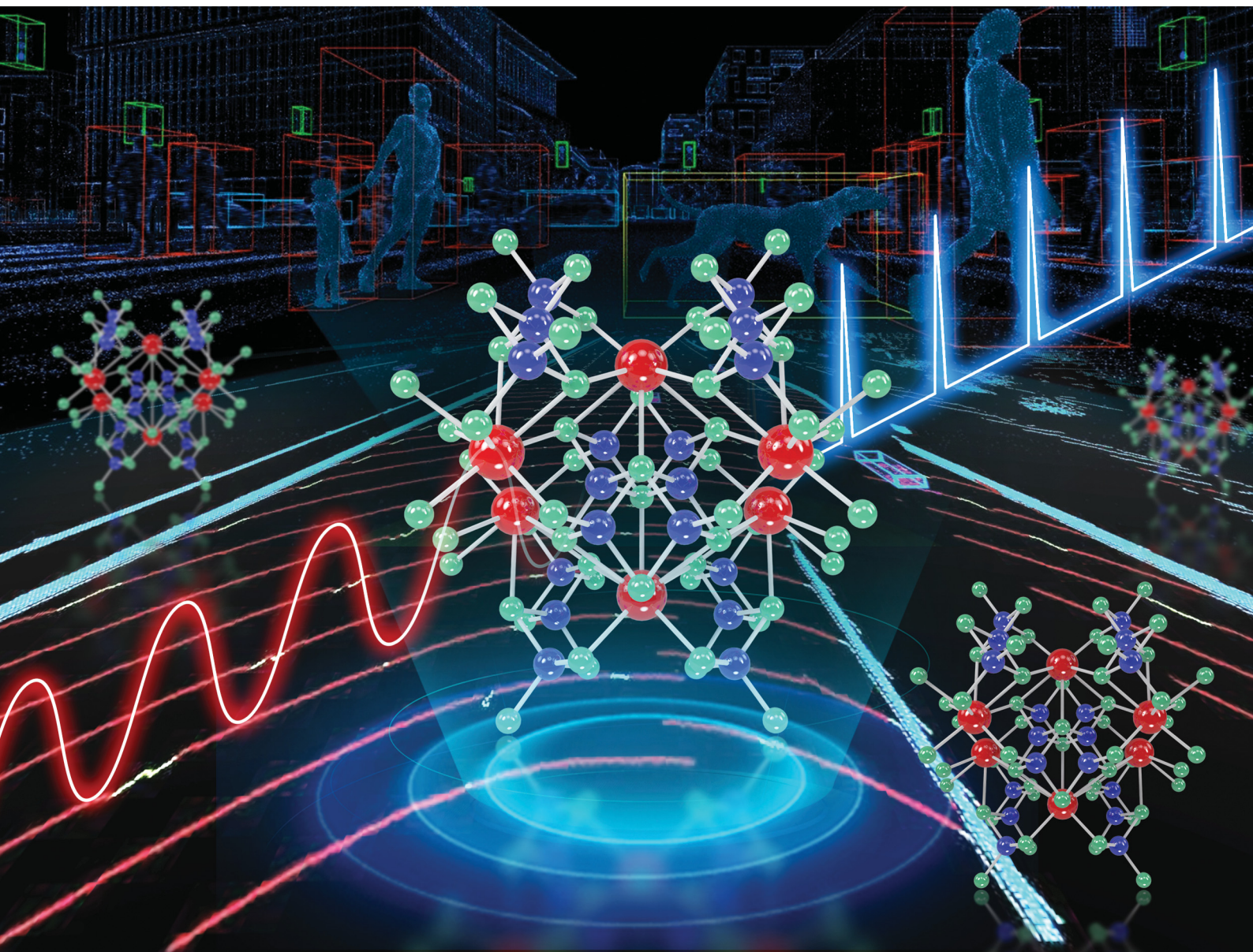
PAPER
Sicong Zhu, Qinglin Zhang, Jian Wu *et al.*
Mode-locking pulse generation based on lead-free halide
perovskite CsCu$_2$I$_3$ micro-rods with high stability

PAPER

Check for updates

Mode-locking pulse generation based on lead-free halide perovskite CsCu₂I₃ micro-rods with high stability†

Haiqin Deng, ‡[a] Xing Xu, ‡[b] Fangqi Liu, ‡[c] Qiang Yu,[ad] Bowang Shu, [ID][a] Zixin Yang,[a] Sicong Zhu, [ID] *[c] Qinglin Zhang, [ID] *[b] Jian Wu [ID] *[a] and Pu Zhou[a]

The industrialization and commercialization of optoelectronic devices require the exploration of novel materials with high stability, nontoxicity, and large-scale manufacturing. The all-inorganic lead-free halide perovskite nanomaterial CsCu₂I₃ has been widely reported in applications in light-emitting diodes (LEDs), photodetectors (PDs), photovoltaics, and so on, due to its good environmental stability and unique optoelectronic properties. However, research on ultrafast photonics has rarely been carried out so far. Here, high quality CsCu₂I₃ micro-rods were fabricated *via* a solvent evaporation crystallization method. The high thermodynamic stability and the broadband response of CsCu₂I₃-based optoelectronic devices have been predicted by density functional theory (DFT), revealing their feasibility for exploitation in fiber laser systems. The nonlinear characteristic of CsCu₂I₃ micro-rods was measured using a balanced twin-detector system, with a modulation depth of 12.04%. Utilizing its remarkable nonlinear optical response and intrinsic stability, a passively mode-locked erbium-doped fiber laser based on a CsCu₂I₃ saturable absorber was achieved. Significantly, the fiber laser could operate stably for at least five months. These experimental results demonstrate that CsCu₂I₃ micro-rods are ultra-stable, and can serve as a promising optical modulation material to produce an ultrafast and long-stability pulse in fiber laser applications.

Introduction

Ultrafast fiber lasers have been proven to be indispensable tools for various crucial applications, such as ultrafast spectroscopy, micromachining, next-generation communication, and intelligent health.[1–4] A saturable absorber (SA) is an important optical component to trigger pulsed operation.[5] Recently, the application of SAs based on novel low-dimensional materials for ultrafast pulse generation has been widely reported, such as graphene,[6–8] carbon nanotubes (CNTs),[9–11] topological insulators (TIs),[12–15] transition metal dichalcogenides (TMDs),[16–19] black phosphorus (BP),[20] and so on.[21–25] Most of them have

unique optical and electrical properties. For instance, graphene possesses zero bandgap, leading to broadband absorption but low modulation depth and weak absorption.[26] BP is suitable for near-infrared optoelectronic applications due to the layer-dependent bandgap from 0.3 eV to 1.5 eV but has poor stability for its oxidation when exposed to an ambient environment, which will shorten the lifetime of optoelectronic devices.[27,28] In addition, to expand the diversity of ultrafast lasers and realize the industrialization applications, we also need to explore new 2D materials with better nonlinear absorption characteristics, facile fabrication, and high stability.

In the past few years, perovskites have also been incorporated into fiber lasers as the SA to generate ultrashort pulses in fiber laser systems, emerging as a promising candidate for novel optoelectronic devices.[29–32] As a representative of the perovskite family, lead halide perovskite nanomaterials have attracted tremendous attention for many appealing properties,[33–36] such as high carrier mobility,[37] tunable bandgaps,[38] high photoluminescence quantum yields, and long carrier diffusion length,[39] which sprung them into a plethora of optoelectronic applications including LEDs,[40,41] solar cells,[42] PDs,[43] nanolasers,[44] and other optoelectronic devices.[45] However, the toxicity of lead-based perovskites and instability against moisture, air, heat, and irradiation have caused significant concern to the ecological

[a] *College of Advanced Interdisciplinary Studies, National University of Defense Technology, Changsha, 410073, China. E-mail: wujian15203@163.com*

[b] *School of Physics and Electronics, Hunan University, Changsha, 410082, China. E-mail: qinglin.zhang@hnu.edu.cn*

[c] *College of Science and Key Laboratory for Ferrous Metallurgy, Resources Utilization of Ministry of Education, Wuhan University of Science and Technology, Wuhan, 430081, China. E-mail: sczhu@wust.edu.cn*

[d] *i-Lab & Key Laboratory of Nanodevices and Applications & Key Laboratory of Nanophotonic Materials and Devices, Suzhou Institute of Nano-Tech and Nano-Bionics, Chinese Academy of Sciences, Suzhou, 215125, China*

‡ These authors contributed equally to this work.

environment and human health, inhibiting the large-scale commercial and scientific applications of lead halide perovskites. Hence, considerable endeavors have been dedicated in recent years to investigating a stable, non-toxic lead-free perovskite and its light-emitting and photovoltaic applications.[46] Recently, ternary copper halide $CsCu_2I_3$, as a member of the perovskite family, has been found to overcome the defects of lead halide perovskite nanomaterials,[47] due to the superior optoelectronic performance including longer carrier diffusion lengths, lower trap densities, non-toxicity and high thermal and moisture stability, showing great potential for industrialization of optoelectronic applications.[48–52] Hence, the research on $CsCu_2I_3$ has recently become a focus. Despite significant advances based on $CsCu_2I_3$ focused on LEDs, PDs, and solar cells,[53–55] the exploration of $CsCu_2I_3$ in ultrafast photonics is still rare.

Recently, perovskite-based SAs have been applied in Q-switching and mode-locking fiber lasers.[31,56–59] Li et al. found that organic–inorganic halide perovskite $CH_3NH_3PbI_3$ exhibited a larger nonlinear absorption coefficient and a low saturable intensity, and demonstrated an ultrafast picosecond pulsed fiber laser based on $CH_3NH_3PbI_3$-SA.[56] Similarly, the SA has also been employed in the erbium-doped fiber (EDF) laser cavity.[57,58] Based on the metal halide perovskite $CsPbBr_3$ quantum dots, Liu et al. obtained stable dissipative soliton pulses in the EDF laser at 1.6 μm.[59] These advances have indicated that perovskite nanomaterials have been developed as an effective SA for ultrafast photonics.

Moreover, the fabrication of $CsCu_2I_3$ micro-rods is a low cost, simple process, and is environmentally friendly, which is more favorable for practical applications. Compared with bulk materials and large films, the morphology of micro-nano columns has unique advantages in optical fiber coupling. Therefore, based on its exceptional properties, $CsCu_2I_3$ can be a good choice as a SA to improve the stability of the fiber laser. Here, a $CsCu_2I_3$-based SA was fabricated by a solvent evaporation crystallization method. The $CsCu_2I_3$ micro-rods as an optoelectronic device are simulated by DFT calculations, which elucidated their superior thermodynamic stability and broadband response. Meanwhile, the $CsCu_2I_3$-based nonlinear test showed a modulation depth of 12.04%. These results demonstrate the feasibility of considering $CsCu_2I_3$ micro-rods as a SA in fiber laser systems. A passively mode-locked fiber laser operating at the communication band is successfully demonstrated. It is worth noting that the fiber laser can operate steadily for at least five months, indicating that the device has ultra-high stability. This research will potentially open up a new pathway for ultrafast photonic applications based on lead-free halide perovskites and provide the possibility for industrial and scientific applications.

Synthesis and characterization of $CsCu_2I_3$ micro-rods

Synthesis of $CsCu_2I_3$ micro-rods

Preparation of $CsCu_2I_3$ precursor solution: the precursor solution was prepared by dissolving 0.13 g CuI (99.9%, Aladdin)

and 0.19 g CsI (99.95%, Aladdin) in 1 mL N,N-dimethylformamide (DMF, 99.8%, Aladdin). After heating the mixed solution to 50 °C and holding it for about 12 hours, the precursor solution was filtered by a polytetrafluoroethylene (PTFE) filter (0.22 μm) to get rid of the undissolved residuum.

Preparation of the $CsCu_2I_3$ micro-rods: at first, a silicon slice was used as a substrate (as shown in Fig. S1, ESI†), which was cleaned by the ultrasonic method with acetone, ethanol, and deionized water, successively. A drop of $CsCu_2I_3$ precursor solution (5 μL) was dropped onto the silicon substrate through a pipette. Then, this substrate was placed on a heating table at ∼50 °C. During the heating process, with the gradual evaporation of the solvent, the solution gradually reached the supersaturated state and the $CsCu_2I_3$ crystals precipitated. After 20–30 min, the solvent evaporated completely and a large number of rod-like structures appeared on the silicon substrate. As schematically shown in Fig. S1 (ESI†), the crystal structure of $CsCu_2I_3$ is formed with the one-dimensional in-line double chains of $[Cu_2I_3]^-$ along the c axis in which the octahedron $[CuI_4]^{3-}$ tetrahedral shared common edges. These chain-like structures are surrounded and isolated by Cs^+ cations.

Characterization of $CsCu_2I_3$ micro-rods

The crystallinity of the samples was confirmed by the X-ray diffraction (XRD) measurements (see Fig. 1(a)). The XRD pattern shows the diffraction peaks of (110), (020), (220), (040), (330), (060), (350), (242), and (080), which match well with the orthorhombic $CsCu_2I_3$ (space group Cmcm, JCPDS, No. 77-0069), indicating that the sample was pure. Additionally, the relatively narrow diffraction peaks also suggest the high crystallization quality of the sample. X-Ray photoelectron spectroscopy (XPS) measurements were performed to verify the elemental composition of the obtained sample. The presence of cesium, copper, and iodine is clearly discernible in the survey XPS spectra (as shown in Fig. 1(b)). The high-resolution XPS spectra of the three elements are displayed in Fig. 1(c–e). There are two peaks at 724.8 and 738.8 eV corresponding to Cs $3d_{5/2}$ and Cs $3d_{3/2}$, and the difference between the two peaks is also consistent with the spin–orbit components (14 eV). From the XPS of Cu 2p, the two spin–orbit peaks located at 932.8 and 952.7 eV without any satellite peaks distinctly reveal the presence of Cu^+ rather than Cu^{2+} in $CsCu_2I_3$. For the I 3d spectrum, the two spin–orbit peaks of I at 619.7 and 631.2 eV correspond to I $3d_{5/2}$ and I $3d_{3/2}$, respectively, which agrees well with other iodide perovskites previously reported. Fig. 1(f) shows the high magnification scanning electron microscopic (SEM) image of $CsCu_2I_3$ micro-rods, demonstrating a relatively smooth surface. Transmission electron microscopy (TEM) was utilized to further investigate the crystal structure of the $CsCu_2I_3$ micro-rods. Fig. 1(g) displays a low-magnification TEM image of a fragment of $CsCu_2I_3$ micro-rods transferred onto a copper grid. The corresponding selected area electron diffraction (SAED) patterns in Fig. 1(h) depict an unambiguous diffraction spot which indicates the single-crystalline properties of the $CsCu_2I_3$ micro-rods. The diffraction spots are confirmed as (200) and (021), which further verify the orthorhombic structure of $CsCu_2I_3$ rods. The SEM image and

This journal is © The Royal Society of Chemistry 2023

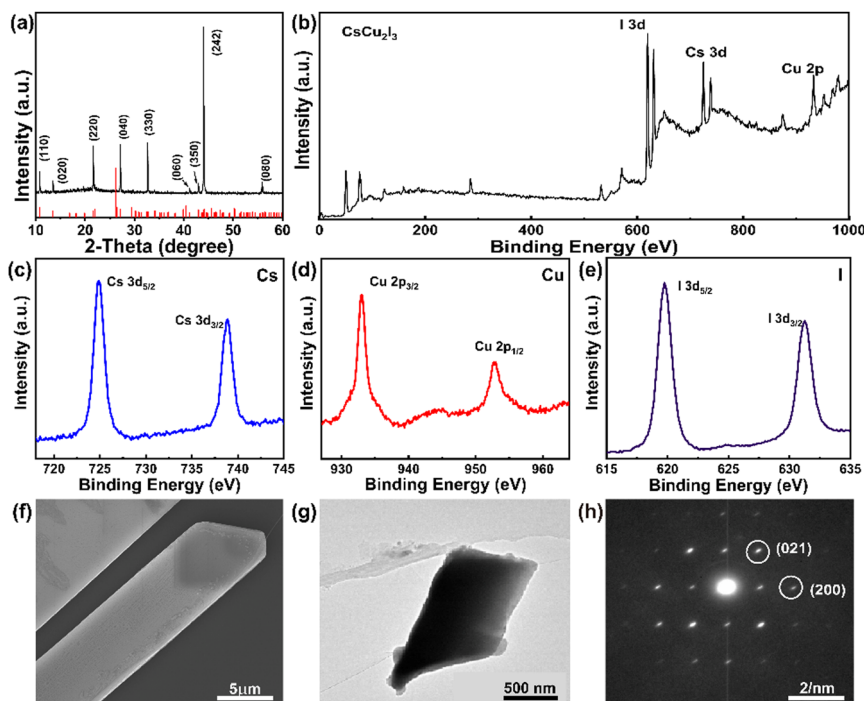*J. Mater. Chem. C*, 2023, **11**, 1696–1703 | **1697**

Fig. 1 Characteristics of $CsCu_2I_3$ crystals. (a) XRD pattern. (b) Total XPS spectrum. (c–e) High-resolution XPS spectra of Cs, Cu, and I, respectively. (f) High magnification SEM image. (g) TEM image. (h) Corresponding SEAD image.

energy-dispersive X-ray spectroscopy (EDS) test of the $CsCu_2I_3$ micro-rods are shown in Fig. S2 (ESI†). The Raman spectrum of the $CsCu_2I_3$ micro-rods shows a characteristic peak at $\sim$116 cm^{-1}, which corresponds to the phonon mode of the I–Cu–I vibration (shown in Fig. S3, ESI†). All these results above demonstrate that the as-grown $CsCu_2I_3$ micro-rods prepared by the solvent evaporation crystallization method are of good quality.

Characteristic evaluation using DFT calculations

In the fiber laser system, as the light passes through the SA, the process of saturating the material with absorbing photons inevitably produces thermal effects. Therefore, the thermodynamic stability of $CsCu_2I_3$ at 300–1500 K is first investigated as shown in Fig. 2(a). It's obvious that the average potential energy of the system within 6 ps maintains $-48\,000$ eV at 300 K-600 K, and there is a dramatic decrease in potential energy at 700 K and it levels off at $-74\,000$ eV as the temperature increases. Although the system's potential energy is certainly affected by the environmental temperature, the standard deviation of the potential energy variation of $CsCu_2I_3$ within 6 ps at different temperatures remained between 0 and 0.5, demonstrating the stability of $CsCu_2I_3$ as a SA (for more details see Fig. S5, ESI†).

In the meantime, the performance of $CsCu_2I_3$ as an optoelectronic device needs further assessment. The constructed model of the $CsCu_2I_3$-based optoelectronic device is shown in Fig. 2(b). The $CsCu_2I_3$ optoelectronic device model consists of three parts, including the left electrode, the central area, and the right electrode. An external bias is applied through the two metal electrodes and the current is measured. When light is

irradiated on a material, photons excite the electrons in the valence band to leap to the conduction band, forming a photocurrent. The photocurrent in each direction under different surface irradiation is studied as shown in Fig. 2(e). It can be seen that there is a continuous absorption peak from the visible to the ultraviolet band, indicating that $CsCu_2I_3$ as a photovoltaic material is capable of a broadband response. And to explain the cause of this phenomenon, the electron leap process behind it is analyzed. The electronic band structure of $CsCu_2I_3$ indicates that the conduction band minimum (CBM) and valence band maximum (VBM) are both located in the G point as shown in Fig. 2(c) and Fig. S6 (ESI†), and the direct gap promotes the effective electron leap. Furthermore, large photocurrents are generated under photon excitation at around 4 eV (red shaded zone) and 6 eV (blue shaded zone) in Fig. 2(e), which can be interpreted in terms of electron transitions between different electron orbitals as shown in Fig. 2(d). The photocurrent peaks in the low energy region are derived from a leap where the electronic states in the red-shaded zone are excited to the ones in the grey-shaded zone. Whereas the photocurrent peaks in the high energy region originate from a transition where the electronic states in the blue-shaded region are excited to the one in the grey-shaded region. The electrons in the blue-shaded zone are significantly more than in the red-shaded zone leading to a larger photocurrent in the high-energy region. The excited electronic state at the valence band is dominated by the d orbital of Cu and the p orbital of I, while the electronic state occupied at the conduction band originates from the d orbital of Cs. Due to the selection rule for the electromagnetic transitions, electrons in the p orbitals are
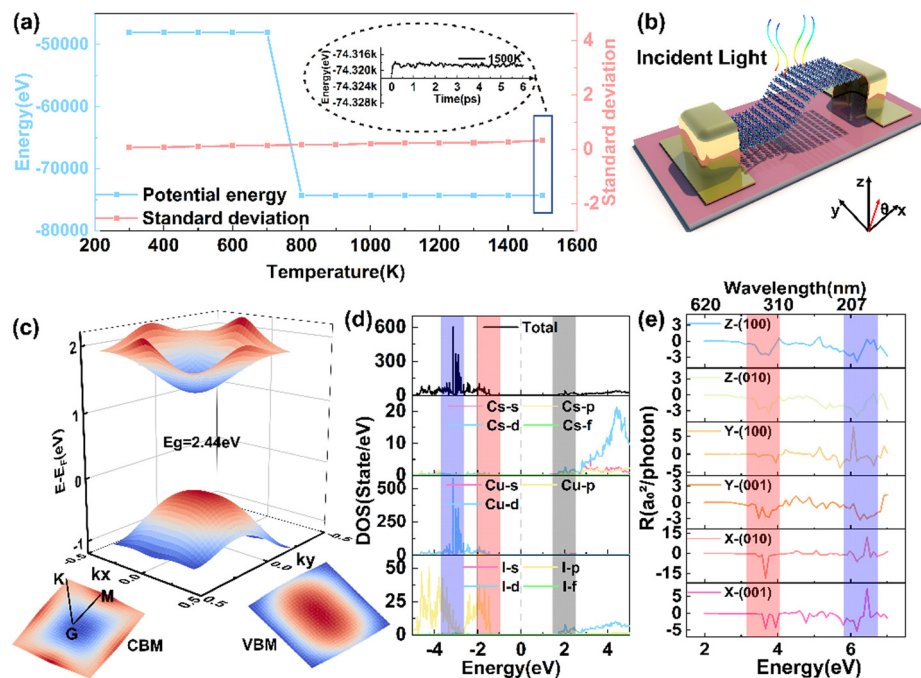
1698 | *J. Mater. Chem. C*, 2023, **11**, 1696–1703

This journal is © The Royal Society of Chemistry 2023

Fig. 2 Thermodynamic stability and electronic band structure of $CsCu_2I_3$. (a) Average system potential energy and standard deviation of energy change within 6 ps for $CsCu_2I_3$ at different temperatures. Right inset: The variation of the potential energy of the system at 1500 K. (b) $CsCu_2I_3$-based optoelectronic device model. (c) 3D views of the CBM and VBM. (d) The density of states of $CsCu_2I_3$ and the contribution of different atomic electron orbitals to the density of states. (e) Photocurrents in different directions (X, Y, and Z) for $CsCu_2I_3$ with different polarization light ((001), (010)).

more likely to leap to the d orbitals thus enhancing the absorption of photons. On the other hand, in fiber laser systems, there are more electronic states at the valence band of $CsCu_2I_3$ than at the conduction band, which leads to rapid saturation of $CsCu_2I_3$ as the SA, favoring the output of the pulse.

Experimental setup and results

Nonlinear optical properties

Considering that the synthesis method of high-quality $CsCu_2I_3$ micro-rods mentioned above is efficient and simple, we apply it to the SA device. As related to the previous method and the schematic diagram (Fig. S1, ESI†), a drop of precursor solution (0.5 μL was dropped onto the fiber end-facet through a pipette. Then, the whole device was dried at 50 °C for 20 min, and the $CsCu_2I_3$ micro-rods appeared on the fiber end-facet of the optic patch cable (SMJ-1315-0.9-0.5m-FU/FU, insertion loss <0.15 dB, return loss >50 dB). After that, the patch cable with $CsCu_2I_3$ micro-rods was connected with a similarly clean one by a terminated fiber adapter. Finally, the SA used in the laser system was successfully prepared. To guarantee that all light in the optical fiber passes through micro-rods, and adjust the mode-locked state conveniently, the material prepared SA must completely cover the core. Fig. S7 (ESI†) indicated that the core of the fiber cable was covered by the $CsCu_2I_3$ micro-rods completely.

The nonlinear optical characteristics of the $CsCu_2I_3$ micro-rods were investigated at 1550 nm (photon energy smaller than the bandgap of $CsCu_2I_3$) by the balanced twin-detector technique, and the experimental device is shown in Fig. S8(a) (ESI†), where

the laser source operated at 1550 nm with a repetition rate of 16.6 MHz and a pulse duration of 448 fs. The corresponding optical transmittance curve of the $CsCu_2I_3$ micro-rods was acquired by the following formula:

$$T(I) = 1 - \Delta T \times \exp\left(-\frac{I}{I_{sat}}\right) - T_{ns} \qquad (1)$$

Here, $T(I)$ refers to the transmittance regarding the input intensity (I), ΔT represents the modulation depth, I_{sat} represents the non-saturable intensity, and T_{ns} represents the non-saturable loss. The experimental data is displayed in Fig. 3(a), showing that as the incident intensity increases, the transmittance increases gradually and then tends to be saturated, showing a typical saturated absorption response. This might be associated with the susceptibility of materials to lattice defects, leading to optical transition, and band filling of intermediate or defective states.[60,61] Hence, the electronic band structures of $CsCu_2I_3$ with Cs, Cu, and I atomic defects are simulated by DFT (as shown in Fig. S9 and S10, ESI†). It's obvious that the VBM of $CsCu_2I_3$ shifts upwards and crosses the Fermi energy level at high solubility defects, and the electronic structure undergoes a transition from semiconductor to metallic behavior. This also supports the application of $CsCu_2I_3$ as SA cooperated into 1.5 μm fiber laser systems. According to eqn (1), by fitting the experimental data in Fig. 3(a), the values of modulation depth, saturated intensity, and non-saturable loss were ~ 12.04%, ~0.19 MW cm^{-2}, and 84.31%, respectively. Therefore, based on the experimental data, the maximum peak power intensity passing through the $CsCu_2I_3$ SA was about 4.089 GW cm^{-2}, and we did not find any optical damage on
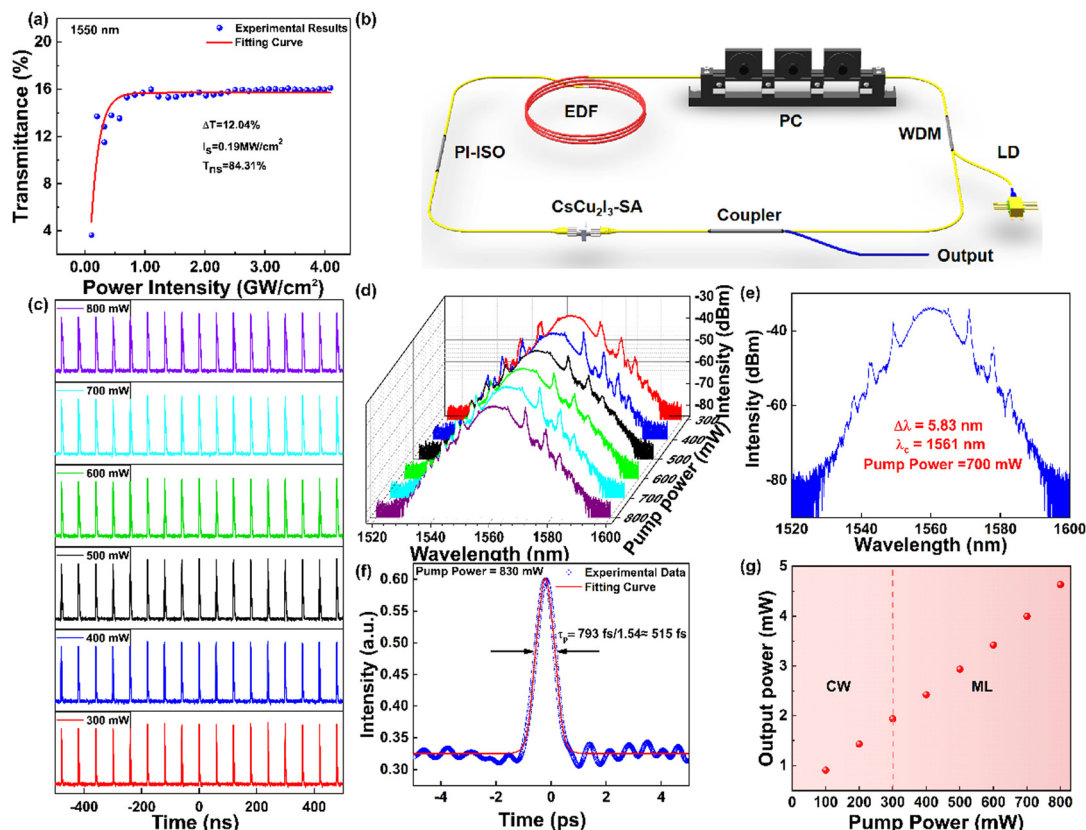
Fig. 3 Characterization of a mode-locked laser based on the CsCu₂I₃-SA. (a) The nonlinear test and fitting results. (b) Configuration of the mode-locking fiber laser. (c and d) Pulse trains and spectrum under different pump powers. (e) Single spectrum under a pump power of 700 mW. (f) Typical autocorrelation trajectory of output pulse at a pump power of 830 mW. (g) Average output power *versus* pump power.

the CsCu₂I₃ SA, which indicates that the damage threshold of CsCu₂I₃ for an ultrafast laser should be larger than 4.089 GW cm⁻². Besides, we further investigated the nonlinear optical properties of CsCu₂I₃ micro-rods at the wavelengths of 1060 nm and 1950 nm by the same method. The corresponding results are shown in Fig. S8(b and c) (ESI†). The modulation depth is about 7.58% at 1 μm and 7.07% at 2 μm, which illustrates that the CsCu₂I₃ micro-rods have great potential for ultrafast photonics.

Fiber laser configuration

The experimental setup of the femtosecond pulse EDF laser based on the CsCu₂I₃-SA is shown in Fig. 3(b). The total length of the cavity is about 12 m with 2.14 m of EDF as the gain medium and 9.86 m of standard single-mode fiber (SMF). The adopted pump source was a 976 nm laser diode (LD, maximum output power of 830 mW), then coupled to the EDF *via* a 980/1550 nm wavelength-division multiplexer (WDM). The polarization controller (PC) was placed between the EDF and the WDM, which can be utilized to manipulate the polarization state in the cavity. A polarization-insensitive isolator (PI-ISO) was inserted after the EDF to ensure unidirectional propagation in case of the backward light's damage. The CsCu₂I₃-SA was placed between the ISO and an optical coupler (OC). Besides, the OC (a 20:80 ratio) was employed to extract the intra-cavity

energy with an 80% portion of laser passed through the CsCu₂I₃-SA and a 20% portion of laser coupled out from the cavity to measure the characteristics of the mode-locked fiber laser. The dispersion coefficients of SMF and EDF are −22 ps² km⁻¹ and 28 ps² km⁻¹, respectively, so the total dispersion is about −0.157 ps².

Results and discussion

On the basis of the aforementioned experimental device, the pulse experiment platform was established. First, the ultrashort pulse was not produced without the CsCu₂I₃-SA, when adjusting the LD pump power from 0 to 830 mW and PC in the whole range. Hence, this clearly indicates that CsCu₂I₃-SA is the crucial component for pulse generation, and the nonlinear polarization rotation (NPR) effect in the resonator is not enough to generate the ultrashort pulse, only the continuous-wave emission, regardless of the pump power and the PC orientation. When the fabricated CsCu₂I₃-SA was inserted into the cavity, mode-locked pulses were acquired when adjusting the pump power in the range of 300–800 mW at an appropriate polarization state. Fig. 3(c) displays the pulse trains under different pump powers, and the adjacent pulse train interval is about 59.8 ns, corresponding to the ring cavity length of 12 m, and a repetition rate of ∼16.7 MHz. The optical spectrum in the range of 300 mW to 800 mW is shown in Fig. 3(d). We can see the spectrum is quite

1700 | *J. Mater. Chem. C*, 2023, **11**, 1696–1703

This journal is © The Royal Society of Chemistry 2023

stable at different pump powers. The corresponding spectrum in stable mode-locking operation shows multistage Kelly sidebands, indicating the pulse is a dispersion-managed soliton. A typical spectrum (as shown in Fig. 3(e)) under a pump power of 700 mW, displays a central wavelength at about 1561 nm and the 3 dB bandwidth at about 5.83 nm. The autocorrelation trace in Fig. 3(f) indicates that single soliton is generated inside the cavity, and the FWHM is about 515 fs, in the case of the incident power set at 830 mW. Fig. 3(g) depicts the output power related to the incident pump power increased monotonically and linearly, implying that the mode-locking fiber laser was stable, and the continuous wave and mode-locking operation are divided by a red dotted line. Hence, according to the data mentioned above, the maximum pulse energy was about 0.28 nJ.

Detailed characteristics of the output pulses are summarized in Fig. 4 with respect to the pump power of 700 mW. The wide-band radio frequency (RF) spectrum is shown in Fig. 4(a), without spurious sidebands in the range of 0–500 MHz, which further manifests the relatively high spectral purity of the mode-locking fiber laser. Moreover, within 0–50 MHz, Fig. 4(b) reveals that the SNR is $\sim$49 dB measured at 16.7 MHz with a resolution bandwidth of 500 Hz. Fig. 4(c) displays the pump power-dependent central wavelength (CW) and 3 dB bandwidth ($\Delta\lambda$). The central wavelength decreases slightly from 1562 nm to 1561 nm with the pump power increasing, indicating the CW has a blue shift. Simultaneously, the 3 dB bandwidth increases from 5.72 nm to 6.01 nm. Fig. 4(d) illustrates the repetition rate is 16.7 MHz and the pulse train interval is 59.8 ns, indicating there were almost no changes with different pump power. Hence, the foregoing data demonstrates that the laser has good performance.

The long-term operational performance of a fiber laser is particularly significant for industrial and scientific applications. Therefore, we have examined the stability of the $CsCu_2I_3$-based mode-locked laser for over 164 days. Fig. 5 displays the general stability test results under a pump power of 700 mW or 800 mW. In the laboratory environment, the pulse laser could run steadily
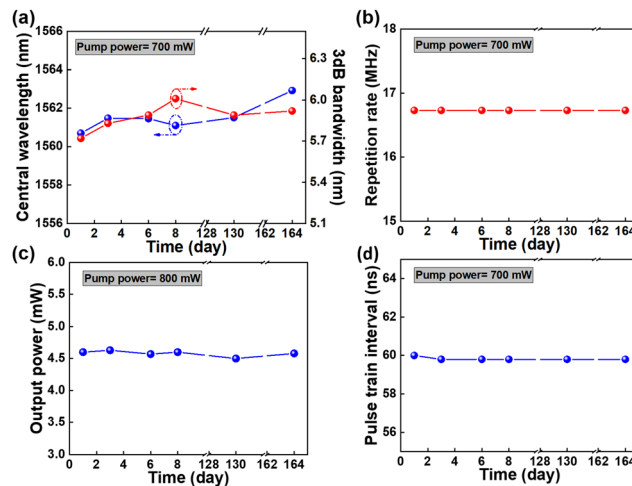
Fig. 5 The robust performance of the mode-locked laser based on $CsCu_2I_3$-SA. The changes of (a) the central wavelength and 3 dB bandwidth, (b) the repetition rate, (c) the output power, and (d) the pulse train interval within 164 days under the same pump power.

for over five months. As shown in Fig. 5(a), the laser spectrum was relatively stable, as the central wavelength varied slowly and the 3 dB bandwidth fluctuated slightly around 5.8 nm, showing a slow rise tendency over time. In Fig. 5(b), the repetition rate has remained unchanged at 16.7 MHz for over five months. The variation of output power and pulse train interval from the average values (Fig. 5(c and d)) were less than 2.6%, and 0.33%, respectively, which shows the laser was very stable within five months. The stability of a SA in ambient air or moisture plays a vital role in the long-life span fiber laser system. Here, the main reasons for the improvement of stability are as follows. On the one hand, according to the reported results,[49,62] Roccanova and Yang et al. have demonstrated the $CsCu_2I_3$ film exhibited good ambient air stability for at least 60 days. Meanwhile, by DFT calculation, we have evaluated the thermal stability at 300–1500 K. Consequently, $CsCu_2I_3$ micro-rods possess good moisture, thermal, and long-term stability. $CsCu_2I_3$-SA, on the other hand, was encapsulated in two fiber optic patch cables, weakening the interaction between $CsCu_2I_3$-SA and air or moisture, and further enhancing its long-term stability. So far, as we know, our pulse laser based on $CsCu_2I_3$-SA shows super stability compared with related results previously reported.

Conclusion

In conclusion, we obtained lead-free perovskite $CsCu_2I_3$ micro-rods by a solvent evaporation crystallization method. By first-principles calculations, we have theoretically demonstrated excellent thermal stability and elucidated the performance of lead-free perovskite $CsCu_2I_3$ micro-rods as an optoelectronic device. As a SA in the fiber laser system, the $CsCu_2I_3$ micro-rods exhibited remarkable nonlinear optical properties with an estimated modulation depth of 12.04%. Hence, a passively mode-locked erbium-doped fiber laser operating at the communication band was proposed with a FWHM of 515 fs at a
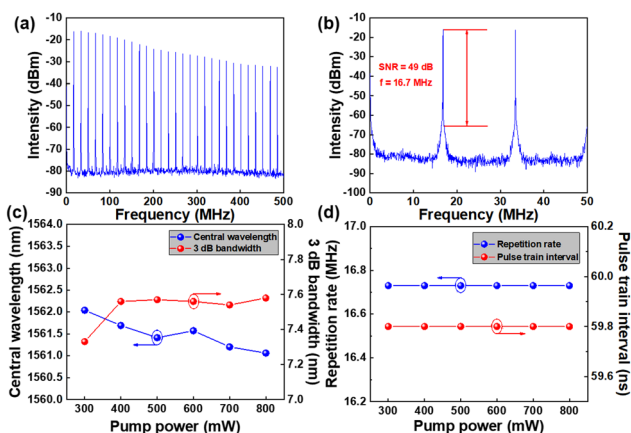
Fig. 4 Performance of the mode-locking laser based on the $CsCu_2I_3$-SA. (a) Recorded RF with a wide span. (b) Narrowband RF Spectrum. (c) Central wavelength and 3 dB bandwidth and (d) repetition rate and pulse train interval as a function of pump power.

repetition rate of 16.7 MHz and a SNR of 49 dB. Then we experimentally demonstrated that the fiber laser possessed high stability, and can operate steadily for at least five months. This research will potentially unlock the pathways for ultrafast photonic and optoelectronic devices based on lead-free halide perovskites.

Author contributions

Haiqin Deng performed the experiments and data processing and wrote the manuscript. Xing Xu synthesized the materials, analysed the TEM, and drew the schematic diagram. Fangqi Liu demonstrated excellent thermal stability and the electronic band structure of $CsCu_2I_3$ by first-principles calculations. Qiang Yu carried out the characterization and analysis of SEM and EDS. Bowang Shu and Zixing Yang revised a part of the manuscript. Sicong Zhu and Jian Wu proposed the idea. Qinglin Zhang and Pu Zhou supervised the project.

Conflicts of interest

The authors have no conflicts to disclose.

Acknowledgements

Notes and references

1 X. Hong, J. Kim, S. Shi, Y. Zhang, C. Jin, Y. Sun, S. Tongay, J. Wu, Y. Zhang and F. Wang, *Nat. Nanotechnol.*, 2014, **9**, 682–686.

2 C. Kerse, H. Kalaycıoğlu, P. Elahi, B. Çetin, D. K. Kesim, Ö. Akçaalan, S. Yavaş, M. D. Aşık, B. Öktem, H. Hoogland, R. Holzwarth and F. Ö. Ilday, *Nature*, 2016, **537**, 84–88.

3 N. G. Horton, K. Wang, D. Kobat, C. G. Clark, F. W. Wise, C. B. Schaffer and C. Xu, *Nat. Photonics*, 2013, **7**, 205–209.

4 E. Agrell, M. Karlsson, A. R. Chraplyvy, D. J. Richardson, P. M. Krummrich, P. Winzer, K. Roberts, J. K. Fischer, S. J. Savory, B. J. Eggleton, M. Secondini, F. R. Kschischang, A. Lord, J. Prat, I. Tomkos, J. E. Bowers, S. Srinivasan, M. Brandt-Pearce and N. Gisin, *J. Opt.*, 2016, **18**, 063002.

5 D. A. Stoliarov, P. A. Itrin, D. A. Korobko, V. A. Ribenek, L. V. Tabulina, A. V. Sysa and Y. P. Shaman, *Opt. Fiber Technol.*, 2021, **63**, 102524.

6 C. Jiang, X. Wang, H. Wang, S. Wang, L. Qin, J. Liu and Z. Zhang, *Adv. Photonics Res.*, 2022, **3**, 2100183.

7 J. Lan, J. Qiao, W. Sung, C. Chen, R. Jhang, S. Lin, L. Ng, G. Liang, M. Wu, L. Tu, C. Cheng, H. Liu and C. Lee, *Nanoscale*, 2020, **12**, 16956–16966.

8 J. Lan, C. Yang, C. Chen, C. Cheng, H. Liu and C. Lee, *J. Mater. Chem. C*, 2022, **10**, 9017–9024.

9 M. Pawliszewska, A. Dużyńska, M. Zdrojek and J. Sotor, *Opt. Express*, 2019, **27**, 11361–11369.

10 J. Wang, Y. Chen and W. J. Blau, *J. Mater. Chem.*, 2009, **19**, 7425–7443.

11 K. K. Chow, S. Yamashita and Y. W. Song, *Opt. Express*, 2009, **17**, 7664–7669.

12 P. Tang, X. Zhang, C. Zhao, Y. Wang, H. Zhang, D. Shen, S. Wen, D. Tang and D. Fan, *IEEE Photonics J.*, 2013, **5**, 1500707.

13 T. Wang, Q. Yu, K. Guo, X. Shi, X. Kan, Y. Xu, J. Wu, K. Zhang and P. Zhou, *Front. Inf. Technol. Electron. Eng.*, 2021, **22**, 287–295.

14 B. Guo, Y. Yao, Y. Yang, Y. Yuan, L. Jin, B. Yan and J. Zhang, *Photonics Res.*, 2015, **3**, 94–99.

15 W. Zhou, X. Pang, H. Zhang, Q. Yu, F. Liu, W. Wang, Y. Zhao, Y. Lu and Z. Yang, *Materials*, 2022, **15**, 6761.

16 S. Lv, X. Liu, X. Li, W. Luo, W. Xu, Z. Shi, Y. Ren, C. Zhang and K. Zhang, *ACS Appl. Mater. Interfaces*, 2020, **12**, 43049–43057.

17 Q. Yu, S. Wang, Y. Zhang, Z. Dong, H. Deng, K. Guo, T. Wang, X. Shi, F. Liu, T. Xian, S. Zhu, J. Wu, Z. Zhang, K. Zhang and L. Zhan, *Nanoscale*, 2021, **13**, 20471–20480.

18 X. Li, J. Feng, W. Mao, F. Yin and J. Jiang, *J. Mater. Chem. C*, 2020, **8**, 14386–14392.

19 Y. Feng, L. Du, Y. He, Q. Yi, J. Li, Q. Duan, S. Chen, L. Miao and C. Zhao, *J. Mater. Chem. C*, 2021, **9**, 6445–6451.

20 Q. Yu, K. Guo, Y. Dai, H. Deng, T. Wang, H. Wu, Y. Xu, X. Shi, J. Wu, K. Zhang and P. Zhou, *J. Phys.: Condens. Matter*, 2021, **33**, 503001.

21 B. Guo, Q. L. Xiao, S. H. Wang and H. Zhang, *Laser Photonics Rev.*, 2019, **13**, 1800327.

22 Z. Ma, H. Zhang, Z. Hu, J. Gan, C. Yang, Z. Luo, T. Qiao, M. Peng, G. Dong, Z. Yang, F. W. Wise and J. Qiu, *J. Mater. Chem. C*, 2018, **6**, 1126–1135.

23 B. Guo, S. Wang, Z. Wu, Z. Wang, D.-H. Wang, H. Huang, F. Zhang, Y. Ge and H. Zhang, *Opt. Express*, 2018, **26**, 22750–22760.

24 J. Wang, T. Wang, X. Shi, J. Wu, Y. Xu, X. Ding, Q. Yu, K. Zhang, P. Zhou and Z. Jiang, *J. Mater. Chem. C*, 2019, **7**, 14625–14631.

25 T. Chai, X. Li, T. Feng, P. Guo, Y. Song, Y. Chen and H. Zhang, *Nanoscale*, 2018, **10**, 17617–17622.

26 B. Zhang, J. Liu, C. Wang, K. Yang, C. Lee, H. Zhang and J. He, *Laser Photonics Rev.*, 2020, **14**, 1900240.

27 M. Tuo, C. Xu, H. Mu, X. Bao, Y. Wang, S. Xiao, W. Ma, L. Li, D. Tang, H. Zhang, M. Premaratne, B. Sun, H.-M. Cheng, S. Li, W. Ren and Q. Bao, *ACS Photonics*, 2018, **5**, 1808–1816.

28 Z. Xie, F. Zhang, Z. Liang, T. Fan, Z. Li, X. Jiang, H. Chen, J. Li and H. Zhang, *Photonics Res.*, 2019, **7**, 494–502.

29 B. Huang, J. Yi, G. Jiang, L. Miao, W. Hu, C. Zhao and S. Wen, *Opt. Mater. Express*, 2017, **7**, 1220–1227.

30 J. Wang, Y. Wang, Z. Chen, X. Yang and R. Lv, *J. Mater. Chem. C*, 2019, **7**, 5047–5050.

31 S. Yang, J. Li, L. Li, L. Zhang and X. Zhang, *J. Mater. Chem. C*, 2022, **10**, 7504–7510.

32 S. Hong, F. Lédée, J. Park, S. Song, H. Lee, Y. S. Lee, B. Kim, D.-I. Yeom, E. Deleporte and K. Oh, *Laser Photonics Rev.*, 2018, **12**, 1800118.

1702 | *J. Mater. Chem. C*, 2023, **11**, 1696–1703

This journal is © The Royal Society of Chemistry 2023

33 M. L. Aubrey, A. Saldivar Valdes, M. R. Filip, B. A. Connor, K. P. Lindquist, J. B. Neaton and H. I. Karunadasa, *Nature*, 2021, **597**, 355–359.

34 M. Liu, Z. Wei, A. Luo, W. Xu and Z. Luo, *Nanophotonics*, 2020, **9**, 2641–2671.

35 K. Sun, D. Tan, X. Fang, X. Xia, D. Lin, J. Song, Y. Lin, Z. Liu, M. Gu, Y. Yue and J. Qiu, *Science*, 2022, **375**, 307–310.

36 D. Marongiu, M. Saba, F. Quochi, A. Mura and G. Bongiovanni, *J. Mater. Chem. C*, 2019, **7**, 12006–12018.

37 F. Yang, A. Wang, S. Yue, W. Du, S. Wang, X. Zhang and X. Liu, *Sci. China Mater.*, 2021, **64**, 2889–2914.

38 G. Xing, N. Mathews, S. S. Lim, N. Yantara, X. Liu, D. Sabba, M. Grätzel, S. Mhaisalkar and T. C. Sum, *Nat. Mater.*, 2014, **13**, 476–480.

39 K. Wei, T. Jiang, Z. Xu, J. Zhou, J. You, Y. Tang, H. Li, R. Chen, X. Zheng, S. Wang, K. Yin, Z. Wang, J. Wang and X. Cheng, *Laser Photonics Rev.*, 2018, **12**, 1800128.

40 S. Liu, Y. Yue, X. Zhang, C. Wang, G. Yang and D. Zhu, *J. Mater. Chem. C*, 2020, **8**, 8374–8379.

41 X. Luo, T. Zheng, Z. Luo, J. Liu, S. Deng, R. Chen, M. Zhang, H. S. Kwok, J. Zhang and G. Li, *ACS Photonics*, 2021, **8**, 3337–3345.

42 S. Tombe, G. Adam, H. Heilbrunner, D. H. Apaydin, C. Ulbricht, N. S. Sariciftci, C. J. Arendse, E. Iwuoha and M. C. Scharber, *J. Mater. Chem. C*, 2017, **5**, 1714–1723.

43 C. Peng, Q. Wei, L. Chen, R. Zeng, Q. Zhang, Q. Hu and B. Zou, *J. Mater. Chem. C*, 2021, **9**, 15522–15529.

44 S. Li, D. Lei, W. Ren, X. Guo, S. Wu, Y. Zhu, A. L. Rogach, M. Chhowalla and A. K. Y. Jen, *Nat. Commun.*, 2020, **11**, 1192.

45 T. Song, Q. Ma, Q. Wang and H. Zhang, *Mater. Adv.*, 2022, **3**, 756–778.

46 R. Khazaeinezhad, S. Hosseinzadeh Kassani, B. Paulson, H. Jeong, J. Gwak, F. Rotermund, D. Yeom and K. Oh, *Sci. Rep.*, 2017, **7**, 41480.

47 X. Xu, C. Fan, Z. Qi, S. Jiang, Q. Xiao, H. Liang, H. Duan and Q. Zhang, *ACS Appl. Nano Mater.*, 2021, **4**, 9625–9634.

48 C. Zhou, T. Zhang, C. Zhang, X. Liu, J. Wang, J. Lin and X. Chen, *Adv. Sci.*, 2022, **9**, 2103491.

49 R. Roccanova, A. Yangui, G. Seo, T. D. Creason, Y. Wu, D. Y. Kim, M. Du and B. Saparov, *ACS Mater. Lett.*, 2019, **1**, 459–465.

50 X. Cheng, S. Yang, B. Cao, X. Tao and Z. Chen, *Adv. Funct. Mater.*, 2020, **30**, 1905021.

51 X. Wang, T. Zhang, Y. Lou and Y. Zhao, *Mater. Chem. Front.*, 2019, **3**, 365–375.

52 R. Lin, Q. Guo, Q. Zhu, Y. Zhu, W. Zheng and F. Huang, *Adv. Mater.*, 2019, **31**, 1905079.

53 F. Sun, T. Liu, P. Ran, X. Chen, T. Jiang, W. Shen, X. Liu and Y. M. Yang, *J. Phys. Chem. Lett.*, 2022, **13**, 3431–3437.

54 X. Xu, S. Jiang, C. Fan, Q. Deng, L. Shen and Q. Zhang, *Adv. Opt. Mater.*, 2022, 2201107.

55 Y. Gu, X. Yao, H. Geng, G. Guan, M. Hu and M. Han, *ACS Appl. Mater. Interfaces*, 2021, **13**, 40798–40805.

56 P. Li, Y. Chen, T. Yang, Z. Wang, H. Lin, Y. Xu, L. Li, H. Mu, B. N. Shivananju, Y. Zhang, Q. Zhang, A. Pan, S. Li, D. Tang, B. Jia, H. Zhang and Q. Bao, *ACS Appl. Mater. Interfaces*, 2017, **9**, 12759–12765.

57 L. Miao, G. Jiang, L. Du, B. Huang, W. Hu, C. Zhao and S. Wen, *IEEE Photonics Technol. Lett.*, 2018, **30**, 1.

58 G. Jiang, L. Miao, J. Yi, B. Huang, W. Peng, Y. Zou, H. Huang, W. Hu, C. Zhao and S. Wen, *Appl. Phys. Lett.*, 2017, **110**, 161111.

59 B. Liu, L. Gao, W. W. Cheng, X. S. Tang, C. Gao, Y. L. Cao, Y. J. Li and T. Zhu, *Opt. Express*, 2018, **26**, 7155–7162.

60 S. Das, Y. Wang, Y. Dai, S. Li and Z. Sun, *Light: Sci. Appl.*, 2021, **10**, 27.

61 X. Zhao, X. Yin, D. Liu, C. Huo, G. Dong, S. Chen, Z. Liu, X. Yan and J. Tian, *J. Phys. Chem. C*, 2022, **126**, 6837–6846.

62 J. Yang, W. Kang, Z. Liu, M. Pi, L. Luo, C. Li, H. Lin, Z. Luo, J. Du, M. Zhou and X. Tang, *J. Phys. Chem. Lett.*, 2020, **11**, 6880–6886.

This journal is © The Royal Society of Chemistry 2023

J. Mater. Chem. C, 2023, **11**, 1696–1703 | **1703**